

Structural analysis of a class III preQ₁ riboswitch reveals an aptamer distant from a ribosome-binding site regulated by fast dynamics

Joseph A. Liberman^a, Krishna C. Suddala^{b,c}, Asaminew Aytenfisu^a, Dalen Chan^d, Ivan A. Belashov^a, Mohammad Salim^a, David H. Mathews^a, Robert C. Spitale^d, Nils G. Walter^b, and Joseph E. Wedekind^{a,1}

^aDepartment of Biochemistry and Biophysics, and Center for RNA Biology, University of Rochester School of Medicine and Dentistry, Rochester, NY 14642; ^bSingle Molecule Analysis Group, Department of Chemistry, University of Michigan, Ann Arbor, MI 48109; ^cBiophysics, University of Michigan, Ann Arbor, MI 48109; and ^dDepartment of Pharmaceutical Sciences, University of California, Irvine, CA 92697

Edited by Thomas R. Cech, University of Colorado, Boulder, CO, and approved June 1, 2015 (received for review February 25, 2015)

PreQ₁-III riboswitches are newly identified RNA elements that control bacterial genes in response to preQ₁ (7-aminomethyl-7-deazaguanine), a precursor to the essential hypermodified tRNA base queuosine. Although numerous riboswitches fold as H-type or HL_{out}-type pseudoknots that integrate ligand-binding and regulatory sequences within a single folded domain, the preQ₁-III riboswitch aptamer forms a HL_{out}-type pseudoknot that does not appear to incorporate its ribosome-binding site (RBS). To understand how this unusual organization confers function, we determined the crystal structure of the class III preQ₁ riboswitch from *Faecalibacterium prausnitzii* at 2.75 Å resolution. PreQ₁ binds tightly ($K_{D,app}$ 6.5 ± 0.5 nM) between helices P1 and P2 of a three-way helical junction wherein the third helix, P4, projects orthogonally from the ligand-binding pocket, exposing its stem-loop to base pair with the 3' RBS. Biochemical analysis, computational modeling, and single-molecule FRET imaging demonstrated that preQ₁ enhances P4 reorientation toward P1-P2, promoting a partially nested, H-type pseudoknot in which the RBS undergoes rapid docking (k_{dock} ~0.6 s⁻¹) and undocking (k_{undock} ~1.1 s⁻¹). Discovery of such dynamic conformational switching provides insight into how a riboswitch with bipartite architecture uses dynamics to modulate expression platform accessibility, thus expanding the known repertoire of gene control strategies used by regulatory RNAs.

preQ₁ riboswitch | gene regulation | crystal structure | single-molecule FRET | molecular dynamics

Riboswitches are structured RNA motifs that sense the cellular levels of small molecules to provide feedback regulation of genes (1). Although present in all domains of life, they are prominent in bacteria where they typically reside in the 5'-leader sequences of mRNA (2). Broad interest in riboswitches originates from the discovery that they can be targeted by antimicrobials (3–5), and the observation that they use complex scaffolds to achieve gene regulation without the need for protein partners. In the latter respect, riboswitches typically exhibit bipartite sequence organization comprising a conserved aptamer linked to a downstream expression platform (2). Aptamer binding to a cognate effector can induce conformational changes that alter the accessibility of expression platform sequences, such as those required for transcriptional read-through, or hybridization to the 16S rRNA as a preface to translation (2, 6).

Numerous riboswitches fold as pseudoknots that conform to the H-type or closely related HL_{out}-type topology, which have emerged as the most efficient RNA scaffolds to integrate aptamer and expression platform sequences (7). The preQ₁-I, preQ₁-II, S-adenosyl-L-methionine-II (SAM-II), and fluoride riboswitches are representative of this organizational strategy, and their analysis has contributed to a renaissance in our understanding of regulatory pseudoknot structure and dynamics (8–18). By contrast, pseudoknotted aptamers that do not integrate their expression platforms are less common, and this added complexity can encumber efforts to elucidate how ligand-induced conformational changes regulate

gene expression. Such riboswitches include the cyclic-di-adenosine monophosphate, SAM-IV, and SAM-I/IV riboswitches (19–22), as well as the recently identified preQ₁-III riboswitch (23).

The discovery of a third class of preQ₁ riboswitches makes this ligand second only to SAM in terms of the number of riboswitches that respond to this effector (23), underscoring the importance of sensing this molecule within the cell (6). PreQ₁ is the last free intermediate on the queuosine (Q) anabolic pathway (Fig. 14). Q is produced exclusively in bacteria (24) where it is incorporated into tRNAs Asn, Asp, His, and Tyr to confer translational fidelity (25–28). Many eukaryotes require Q but attain it as the base queuine from gut flora or diet (29); its deficiency in germ-free mice compromises tyrosine production (30). In bacteria, Q elimination diminishes growth fitness in stationary phase (24), and can contribute to virulence loss (31). At present, the preQ₁-III riboswitch has been identified in a handful of Ruminococcaceae with the preponderance of sequences originating from metagenomes (23). The proximity of the aptamer to a downstream RBS preceding the *queT* start codon suggests a role in translational regulation comparable to many class I, and all class II preQ₁ riboswitches (23, 32, 33). However, at ~100 nucleotides in length, the preQ₁-III riboswitch is substantially larger than other family members, which exhibit more diminutive sizes ranging from 33 to 58 nucleotides. Moreover, the preQ₁-III aptamer domain is

Significance

Riboswitches are RNA molecules found mostly in bacteria that control genes by sensing cellular levels of metabolites, such as the simple organic compound preQ₁. The diversity of riboswitches and their potential as novel antibiotic targets continue to elicit interest in these regulatory sequences. Here we present the crystal structure of a newly discovered bacterial preQ₁-III riboswitch that senses preQ₁ using an unusual, two-part architecture. A complementary analysis of flexibility and dynamics showed that recognition of preQ₁ induces riboswitch compaction, while concomitantly enhancing formation of a distant double-helix possessing a regulatory signal that zips and unzips rapidly, producing gene “off” and “on” states. These observations expand our knowledge of riboswitch construction and suggest a broader role for dynamics than previously recognized.

Author contributions: D.H.M., N.G.W., and J.E.W. designed research; J.A.L., K.C.S., A.A., D.C., I.A.B., M.S., R.C.S., and J.E.W. performed research; J.A.L., K.C.S., A.A., D.H.M., R.C.S., N.G.W., and J.E.W. analyzed data; and K.C.S., N.G.W., and J.E.W. wrote the paper.

The authors declare no conflict of interest.

This article is a PNAS Direct Submission.

Data deposition: The atomic coordinates have been deposited in the Protein Data Bank, www.pdb.org (PDB ID code 4RZD).

¹To whom correspondence should be addressed. Email: joseph.wedekind@rochester.edu.

This article contains supporting information online at www.pnas.org/lookup/suppl/doi:10.1073/pnas.1503955112/-DCSupplemental.

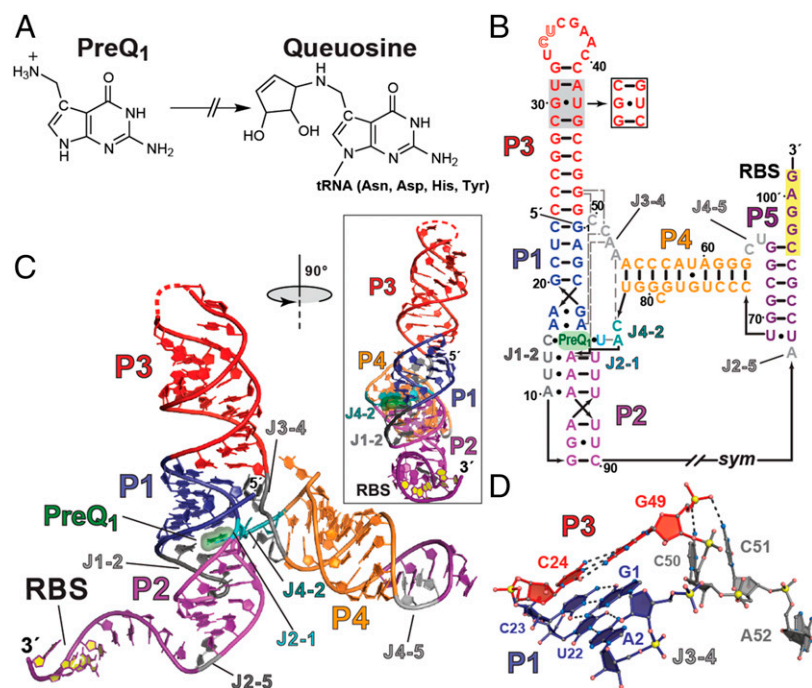


Fig. 1. Queuosine biosynthesis, secondary structure, and overall fold of the ligand-bound preQ₁-III riboswitch. (A) Biosynthesis of the hypermodified nucleotide queuosine (Q) begins with GTP and leads to the intermediate preQ₁ via enzymes of the *queCDEF* operon, which is regulated by a preQ₁-I riboswitch in some bacteria (33). PreQ₁ is then inserted at the wobble position of specific tRNAs with additional modifications added in situ (the complete pathway is reviewed in ref. 52). A scavenging pathway has been proposed wherein Q-related molecules are imported by the *queT* (COG4708) gene product (32), which is regulated in some bacteria by class I, II, and III preQ₁ riboswitches. (B) Secondary structure of the wild-type *F. prausnitzii* riboswitch based on the crystal structure. PreQ₁ is green, junctions are labeled J, and pairing regions (P) are color-coded; long-range interactions are indicated by dashed lines. A boxed sequence (gray) near P3 indicates the sequence used to produce a phasing module (PM) (53). The RBS sequence 5'-CGGAG-3' is highlighted (yellow). The assigned secondary structure differs subtly from comparative sequence analysis (23) because the U17•A84 interaction is not a canonical pair. The *sym* label indicates the crystallographic domain-swapping interaction that resembles bioinformatically predicted helix P5. (C) Cartoon of the preQ₁-bound crystal structure preserving colors from B; preQ₁ is depicted as a semitransparent surface model. The RBS sugar and base rings are yellow. (Inset) View from C rotated 90° about the y axis. (D) Coaxial stacking of P1 with the proximal end of helix P3, and depiction of P3 to J3-4 tertiary contacts.

confined to an atypically organized HL_{out}-type pseudoknot that does not appear to incorporate its downstream expression platform. Biochemical analysis has not identified the location or mode of preQ₁ binding, and the backbone flexibility of both RBS and anti-RBS sequences did not modulate appreciably as a function of preQ₁ concentration (23), unlike class I and II preQ₁ riboswitches that show clear preQ₁-dependent RBS sequestration (16, 18, 32, 33).

To elucidate the molecular basis for ligand recognition and translational regulation by the class III preQ₁ riboswitch, we determined the crystal structure of the intact sensing domain from *Faecalibacterium prausnitzii* in complex with preQ₁ at 2.75 Å resolution. We used isothermal titration calorimetry (ITC), chemical modification (selective 2'-hydroxyl acylation analyzed by primer extension, or SHAPE), computational modeling, and single-molecule FRET (smFRET) analyses to relate the atomic-level details of ligand binding to conformational dynamics. Our results show how preQ₁ binding within an atypically organized HL_{out}-type pseudoknot can promote a globally compact fold. This conformation increases the population of molecules competent to form a second downstream pseudoknot, wherein the RBS docks dynamically within a helix distal to the aptamer domain. The discovery of such rapidly interconverting conformational states broadens our understanding of regulatory RNA structure, and supports a new role for dynamics in riboswitch-mediated control of protein translation.

Results

Ligand Binding and Bipartite Organization of the PreQ₁-III Riboswitch Structure. The *F. prausnitzii* riboswitch of this investigation comprises 101 nucleotides of the wild-type sequence encom-

passing the predicted 5' pseudoknot and the 3' RBS (23) (Fig. 1B). This construct binds preQ₁ with an apparent K_D of 6.5 ± 0.5 nM and a binding stoichiometry of 1:1 (Table S1 and Fig. S14; Methods and SI Methods). These results are comparable to values measured for class I and II family members, which produced apparent K_D values of 7.3 nM and 17.9 nM, respectively, and showed similar 1:1 binding stoichiometry (11, 18). Crystals of the 101-mer were grown from organic salts at neutral pH and the phase problem was overcome by single-isomorphous replacement with anomalous scattering; the initial structure was then refined to 2.75 Å resolution to acceptable R_{factor} and geometry values (Table 1). The global tertiary fold is λ-shaped with dimensions of $92 \times 80 \times 32$ Å (Fig. 1C). The aptamer is composed of contributions from four pairing regions, P1–P4 (Fig. 1B and C), organized as a HL_{out}-type pseudoknot wherein P3 and P4 reside in extended loop, L3, located in the 3' tail (Fig. S24). P1 is longer than predicted (23) because consecutive purines form *trans* Watson–Crick pairs that extend this helix (Fig. 1B and C). This conserved feature allows P1 insertion between P2 and P3, forming a coaxial stack that becomes continuous when preQ₁ binds in the pocket formed by the P1–P2–P4 helical junction (Fig. 1B and C). The stacked P1–P3 feature (Fig. 1D) clarifies why mutations that disrupted the proximal end of P3 led to reduced ligand affinity, whereas distal mutations within this helix showed only nominal effects (23). P4 projects orthogonally from the P2–P1–P3 coaxial stack, forming a 43-Å-long helix whose stem-loop is complementary in sequence to the 3' terminus of the riboswitch (Fig. 1B and C). However, rather than engaging in the 7-bp helix predicted by bioinformatics (23), the

Table 1. PreQ₁-III X-ray diffraction and refinement statistics

Samples	PM (native)	PM (0.1 M CsCl)	Wild-type (refinement)
Data collection*			
Wavelength, Å	1.0000	1.7000	1.1696
Space group	P6 ₅ 22	P6 ₅ 22	P6 ₅ 22
Cell constants			
<i>a</i> = <i>b</i> , <i>c</i> , Å	83.7, 278.7	83.8, 279.8	84.1, 278.4
α = β , γ , °	90.0, 120.0	90.0, 120.0	90.0, 120.0
Resolution (Å)	41.40–3.00 (3.10–3.00)	44.30–3.00 (3.10–3.00)	39.20–2.75 (2.90–2.75)
<i>R</i> _{p.i.m.} (%)†	4.5 (11.7)	3.0 (11.9)	3.9 (97.8)
CC1/2 (%)‡	99.7 (97.6)	99.9 (99.6)	99.9 (58.0)
<i>I</i> / σ (<i>I</i>)	15.6 (2.3)	22.9 (2.7)	16.6 (0.9)
Complete (%)	98.8 (93.8)	96.0 (74.5)	97.1 (99.1)
Redundancy	8.0 (7.5)	18.8 (8.0)	3.0 (3.1)
Refinement statistics			
Resolution, Å			38.3–2.75
No. reflections			14,702
<i>R</i> _{work} / <i>R</i> _{free} , %			21.2/22.8
No. atoms			
RNA			2,119
Ligand			13
Water			4
B-factors, Å²			
RNA			122
Ligand			60
Water			90
Rmsd			
Bonds, Å			0.002
Angles, °			0.55
Clash score [§]			1.24
Coord. error, Å [§]			0.46

*X-ray data collection was conducted remotely at the SSRL using Blu-ICE software and the Stanford Auto-Mounter (48).

† $R_{\text{precision-indicating merging } R\text{-value}} = \frac{\sum_{hkl} \sqrt{\frac{1}{N-1} \sum_{i=1}^N |I(hkl) - \langle I(hkl) \rangle|}}{\sum_{hkl} \sum_{i=1}^N I(hkl)}$, where *N* is the redundancy of the data and $\langle I(hkl) \rangle$ is the average intensity (49).

‡The Pearson correlation coefficient calculated for the average intensities resulting from division of the unmerged data into two parts, each containing half of the measurements selected at random for each unique reflection (50).

§As implemented in PHENIX (51).

P4 stem-loop pairs intermolecularly (Fig. 1*B*). This domain-swapped interaction appears to have facilitated crystallization and mimics aspects of the predicted intramolecular RBS base pairing interaction believed to be operative in gene regulation (23) (see below).

Ligand Recognition Uses Base Triples and Inclined A-Minor Interactions. PreQ₁ binding occurs within the P1–P2–P4 helical junction at the P1–P2 interface, stitched together by J1-2 and J2-1 (Fig. 2*A*). The closing P1 pair, A6•A18, forms the “ceiling” of the binding pocket, and the U8•A85–U16 triplex serves as the floor. The quality of the riboswitch model is demonstrated by the fit of preQ₁ into electron density maps that define its orientation and chemical contacts, including a hydrogen bond and salt bridge to the preQ₁ methylamine moiety from O2 of U8 and the *pro*-R_p nonbridging oxygen of A85 (Fig. 2*B* and Fig. S3*A*). Junction nucleotides contribute a belt of equatorial interactions to the effector. C7 of J1-2 forms a *trans* Watson–Crick interaction with the guanine-like face of preQ₁, whereas U17 of J2-1 engages the “minor groove” edge (Fig. 2*A* and *B*). The A52 and A84 N1 imines accept hydrogen bonds from the 2'-OH groups of A85 and U17 (Fig. 2*A* and *B*). These inclined A-minor interactions originate from the

extended 3' tail of the HL_{out}-type pseudoknot and provide base stacking interactions that buttress the binding-pocket floor and ligand, respectively (Fig. 2*A* and *B*). With regard to the floor, prior bioinformatic and biochemical analyses predicted P2 formation with caution due to its lack of covariation and A-U richness (23). These attributes are explained by the structure because bases U8 through A10 of J1-2 form major-groove triplexes with the Hoogsteen edges of bases A85–A87, stabilizing the P2 helix while fortifying the pocket floor (Fig. 2*C*). The identification of consecutive U•A-U triples in the structure also explains why prior U14-A87 and U15-A86 transversion mutations lowered preQ₁ affinity (23). Overall, the quadruple triplex motif provides a stable, flat surface to recognize the mostly planar preQ₁ ligand, whose presence is integral to the formation of a stable P2–P1–P3 coaxial stack (Fig. 1*B* and *C* and Fig. S2*A*).

Base Triples of the PreQ₁-III Aptamer Exhibit Similarities to the Ligand-Recognition Motifs of Other Riboswitches. Use of major-groove base triples for effector recognition is a molecular motif that the preQ₁-III riboswitch shares with a handful of other regulatory RNAs. The preQ₁-II and preQ₁-III riboswitches recognize preQ₁ by using a common constellation of bases and underlying U•A-U triplexes that superimpose with an rmsd of 1.1 Å (Fig. 3*A*). A notable difference in this comparison is that the hydrogen-bonding pattern between N1 of preQ₁ and the Watson–Crick face of C8 in the preQ₁-II riboswitch is consistent with bifurcation (12). This mode of imine hydrogen bonding by the ligand is not evident in the preQ₁-III structure, and appears to be a source of positional differences in the respective structures (Fig. 3*A*). Interestingly, the SAM-II riboswitch uses a similar array of major-groove triples to recognize the adenine moiety of SAM (8) (Fig. 3*B*); these nucleotides superimpose on the triplexes of the preQ₁-III riboswitch with an rmsd of 0.82 Å. SAM overlaps U17 of the preQ₁-III riboswitch in the C7•preQ₁•U17 triplet, whereas preQ₁ overlaps U44 of the U10•U44•SAM triplet. Beyond variations in the ligand-recognition triplex, the underlying U•A-U triples of the preQ₁-II, preQ₁-III, and SAM-II riboswitches show substantial spatial similarity (Fig. 3*A* and *B*). The cyclic-di-guanosine-monophosphate-II (c-di-GMP-II) riboswitch also uses major-groove triples to bind the guanine bases of its ligand (34), and produces a local superposition of 2.0 Å compared with the preQ₁-III riboswitch (Fig. 3*C*). This degree of structural homology is noteworthy given the fact that these riboswitches do not share any common bases in this region. In light of the distinct evolutionary origins and diverse tertiary folds of the riboswitches examined here, this analysis highlights the resilience and versatility of triplexes in the recognition of nucleobase ligands, which should facilitate prediction of regulatory RNA function based on sequence.

Thermodynamic Analysis of PreQ₁ Binding-Site Mutants Supports the Observed Mode of Ligand Recognition. To evaluate the thermodynamics of folding, divalent ion requirements, and to validate the structural basis of preQ₁ recognition by the preQ₁-III riboswitch, we conducted a series of binding experiments in solution using ITC. Effector binding by the preQ₁-III riboswitch is enthalpy driven with a ΔH of -26.8 ± 0.2 kcal·mol⁻¹, which more than offsets the unfavorable entropy of 15.8 ± 0.2 kcal·mol⁻¹ (Table S1). Prior in-line probing experiments on the wild-type *Fpr* riboswitch sequence used in this investigation (23), as well as ITC analysis on a second, minimal preQ₁-III riboswitch, env 74 (Fig. S4*A*), indicated that the 3' tail of the riboswitch is dispensable past P2 for preQ₁ binding (Table S1 and Fig. S1*B* and *C*); these results agree with the crystal structure wherein the 3' terminus is not involved in aptamer formation. Site-bound divalent metal ions were not observed in the preQ₁-III crystal structure, and the riboswitch binds preQ₁ in the absence of Mg²⁺, albeit with a reduction of affinity by a factor of three, and a substoichiometric

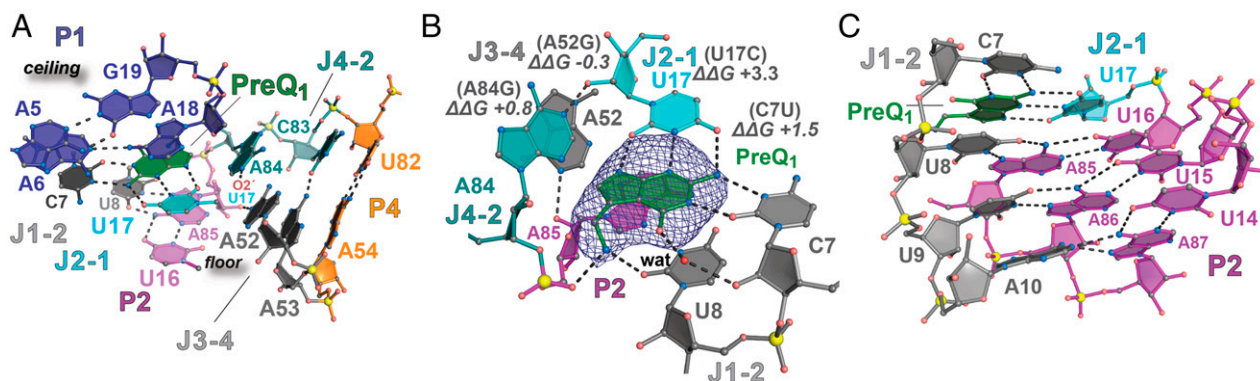


Fig. 2. Details of the preQ₁-binding pocket within a three-helix junction. (A) Close-up view of the P1–P2–P4 helical junction that binds preQ₁. The “ceiling” exhibits tandem purine base pairs emanating from P1. PreQ₁ resides in the center of a base triple flanked by C7 and U17. Stacked bases A84 and A52 make respective N1-imino to 2'-hydroxyl group interactions with U17 and A85; the latter base stacks below preQ₁ as part of the U•A-U triplex that composes the pocket “floor.” (B) Close-up view of the preQ₁-binding site depicting the final refined ligand bathed in unbiased (average kicked) $mF_o - DF_c$ electron density at the 3.0σ level. Ligand-specific readout by C7 and U17 is shown in the context of the U8•A85 Hoogsteen pair that forms the floor. The A85 phosphate group and O2 keto of U8 make complementary interactions to the 7-aminomethyl moiety of preQ₁, providing additional specificity. $\Delta\Delta G$ (kcal·mol⁻¹) values relative to wild type are shown for various mutations tested for ligand binding (Table S1). The view is rotated $\sim 180^\circ$ about the y axis relative to Fig. 1C. (C) Major-groove base-triple pairing of J1-2 with P2 under the preQ₁-binding pocket; tandem U•A-U triples are flanked by a single A10•A87-U14 triplex.

n value of 0.64 (Table S1 and Fig. S1D). These observations imply that divalent ions are important for proper preQ₁-III riboswitch folding, which could be the underlying cause of reduced ligand recognition. We then analyzed various mutants of specific nucleobases observed in the structure to be important for preQ₁ binding. C7U yielded a $\Delta\Delta G$ of 1.5 kcal·mol⁻¹ compared with wild type, suggesting one or two lost hydrogen bonds in accord with the structure (Fig. 2B, Fig. S1E, and Table S1). U17C produced a $\Delta\Delta G$ of 3.3 kcal·mol⁻¹ (Fig. S1F and Table S1), implying two or three lost hydrogen bonds to preQ₁, which also concurs with the structure (Fig. 2B). The inclined A-minor bases A52 and A84 do not hydrogen bond directly to preQ₁ and, accordingly, the respective A-to-G mutations showed smaller $\Delta\Delta G$ values of -0.3 kcal·mol⁻¹ and 0.8 kcal·mol⁻¹ (Fig. 2B, Table S1, and Fig. S1G and H). We hypothesize that such free-energy changes are the result of interactions gained and lost. A52G adds an exocyclic amine on its sugar edge that likely serves as a hydrogen bond donor to both the N3 and the 2'-OH of A85 in the binding-pocket floor. These favorable contacts would form at the expense of the wild-type A-minor interaction while offsetting suboptimal base stacking against the binding pocket, consistent with the modestly favorable $\Delta\Delta G$ of -0.3 kcal·mol⁻¹. By contrast, the A84G mutant adds a bulky N2 amine that likely forms a hydrogen bond with the 2'-OH of U17, albeit at the expense of the wild-type A-minor interaction. Beyond this com-

pensatory interaction, the net unfavorable $\Delta\Delta G$ (i.e., 0.8 kcal·mol⁻¹) could be the result of suboptimal π stacking with the pyrrole ring of the ligand. Overall, these findings have implications for the means by which ligand binding in the aptamer predisposes the expression platform to adopt gene regulatory conformations (discussed below).

SHAPE Reactivity Changes Are Confined to the Core of the PreQ₁-III Aptamer. To explore how preQ₁ binding influences RNA backbone flexibility in solution, we performed SHAPE analysis on the wild-type *Fpr* preQ₁-III riboswitch in the context of a sequencing cassette (Fig. S4B). The addition of preQ₁ to the riboswitch reduced reactivity at several positions, including P1, the U-rich region of P2, J3-4, and positions 84 and 86 (Fig. 4A and B). Differential SHAPE-reactivity analysis showed strong P1 and P2 modulation (Fig. 4C), consistent with the crystal structure in which preQ₁ mediates coaxial stacking between these helices (Figs. 1C and 2A). Nucleotides that contact preQ₁ in the three-way junction also showed modulation, including C7 of J1-2, which recognizes the effector, and U8 of the major-groove triple located in the floor of the binding pocket (Fig. 2A); U17 of J2-1, which directly recognizes the preQ₁ edge (Fig. 2B); A52 of J3-4, which contributes an inclined A-minor interaction to the binding pocket on one face, and base stacking upon A53 with the other (Fig. 2A and B); and A84 of J4-2, which contributes a second inclined A-minor interaction that directly abuts preQ₁

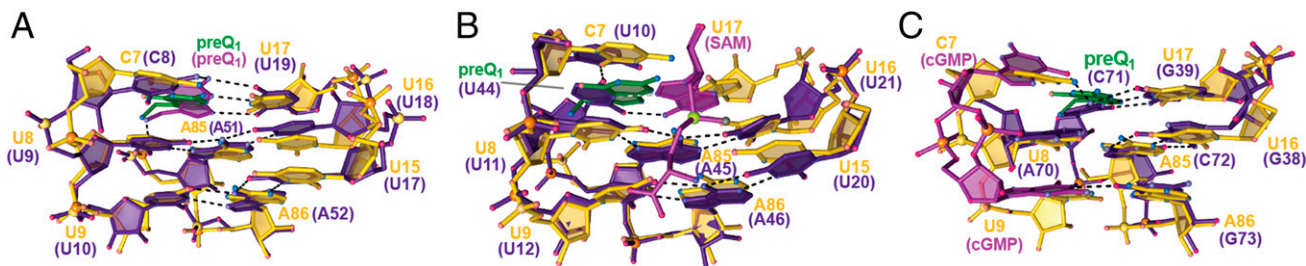


Fig. 3. Comparison of the preQ₁-III riboswitch to other regulatory RNAs that use triplexes to recognize nucleobase ligands. (A) Overlay of the preQ₁-III riboswitch base triples (gold) upon the preQ₁-II riboswitch (deep purple; PDB ID code 2MIY) (12). The superposition is based on the major-groove base triples and preQ₁, which yielded an average rmsd of 1.1 Å. Here and elsewhere, the preQ₁-III riboswitch ligand is green, and the superimposed ligand is magenta. (B) Overlay of the preQ₁-III riboswitch base triples upon those of the SAM-II riboswitch (deep purple; PDB ID code 2QWY) (8). The superposition is based on shared major-groove base triple nucleotides (excluding ligand), which yielded an average rmsd of 0.82 Å. (C) Overlay of the preQ₁-III riboswitch base triples with those of the c-di-GMP-II riboswitch (deep purple; PDB ID code 3Q3Z) (34). The superposition is based on shared nucleotide atoms (excluding ligand), which yielded an average rmsd of 2.0 Å.

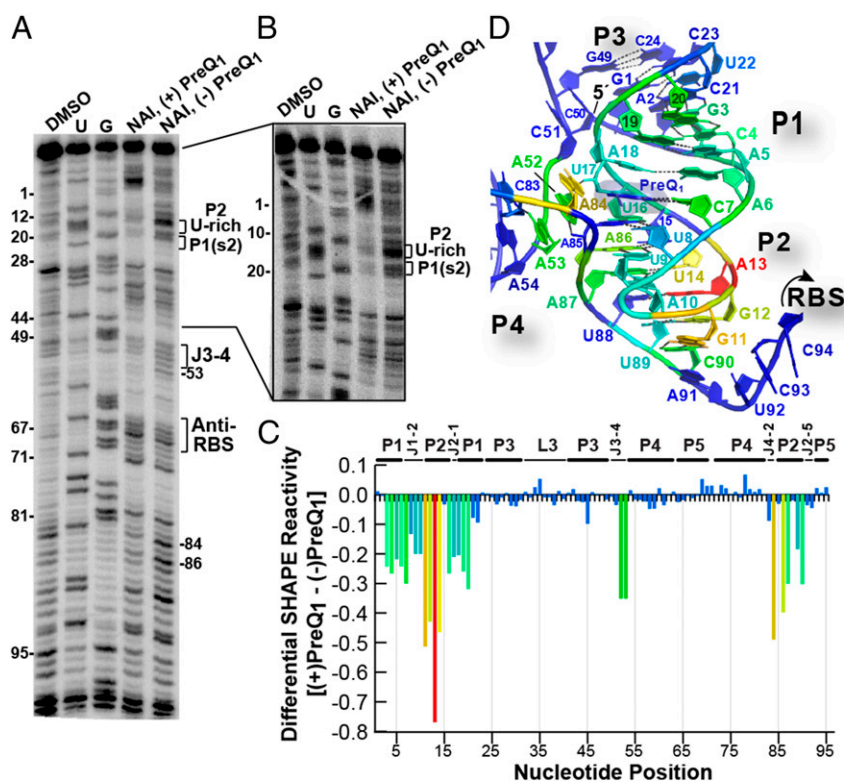


Fig. 4. Representative ligand dependence of 2'-OH chemical modification for the wild-type preQ₁-III riboswitch. (A) Electrophoretic SHAPE analysis conducted in the absence and presence of preQ₁ using the chemical modification reagent NAI; DMSO represents a control without NAI; U and G indicate reference nucleotide sequences. P1(s2) represents the 3'-most strand of helix P1; anti-RBS represents the P4 loop predicted to pair within helix P5; (-)preQ₁ indicates no ligand and added NAI; (+)preQ₁ indicates 100 μM ligand and added NAI. (B) High-resolution analysis of the 5'-riboswitch sequence similar to A, but emphasizing changes in P1 and P2 in the absence and presence of ligand. (C) Differential SHAPE reactivity as a function of nucleotide position. Reactivity is shown as a heat map; dark blue indicates little or no change; red indicates large differences between ligand bound and free states. (D) The crystal structure of the preQ₁-III riboswitch (Fig. 1C) showing the spatial distribution of differential SHAPE reactivity using the heat map from C.

(Fig. 2A and B). Structural mapping of the differential SHAPE reactivity revealed that most changes occur within the three-way helical junction that composes the effector-binding site (Fig. 4D), suggesting that preQ₁ reduces core backbone flexibility while promoting the HL_{out}-type pseudoknot fold. By contrast, P3 and P4 are largely unaffected by preQ₁, implying that they are pre-folded. Perhaps the most surprising observation was the apparent lack of preQ₁-dependent modulation within the anti-RBS and RBS sequences (i.e., helix P5; Fig. 4A and C). This result prompted us to explore the feasibility of P5 helix formation by use of computational approaches.

Computational Modeling Demonstrates the Structural Feasibility of RBS Sequestration. The preQ₁-I and preQ₁-II riboswitches fold as pseudoknots that partially or fully integrate their expression platforms into the aptamer core (Fig. S2B and C), features commonly observed in riboswitches that adopt H- and HL_{out}-type pseudoknot architectures (7). By contrast, the preQ₁-III riboswitch does not incorporate its expression platform into the aptamer, which folds as an HL_{out}-type pseudoknot that is extended significantly in its “L3 loop” due to the inclusion of helix P3 (Fig. S2A). The most parsimonious pathway to achieve translational regulation by the preQ₁-III riboswitch entails ligand-dependent sequestration of the RBS via formation of the P5 helix in the expression platform located distally from the aptamer domain. Although we identified a 3' helix involving the RBS, its mode of burial in the crystal structure involves two molecules (Fig. 1B and Fig. S3D and E), resulting in a base-pairing pattern inconsistent with bioinformatic analysis (23). Therefore, we used a computational approach to test the feasi-

bility of producing an intramolecular P5 helix based on the crystal structure. Our results demonstrate that a “gene-off” conformation is readily attainable through burial of the RBS within helix P5, which forms the second stem of a partially nested H-type pseudoknot that encompasses the expression platform (Fig. 5A and Fig. S5A). Although the preQ₁-III riboswitch model retains an intact HL_{out}-type pseudoknot aptamer bound to preQ₁, formation of helix P5 necessitates acute reorientation of helix P4 toward P2 (Fig. S5B and C). Nevertheless, the model still accounts for the observed ITC and SHAPE measurements (Figs. 2B and 4D). Inspection of the 7-bp helix of P5 reveals three RBS nucleotides engage in canonical or wobble base-pair interactions, whereas the last two bases stack upon helix P5 (Fig. 5B). The model also concurs with bioinformatic sequence results that show conservation of P5 bases, but poor conservation of flanking bases in unpaired regions (23) (Fig. 5B, Inset). Although the model of the ligand-bound preQ₁-III riboswitch shows considerable conformational flexibility during unrestrained MD simulations spanning 8 μs, P5 atoms showed little positional variation, supporting the stability of this helix on a microsecond timescale (Fig. S5D and E).

Single-Molecule FRET Supports Dynamic RBS Sequestration upon preQ₁ Binding. To understand how ligand binding promotes RBS sequestration, we conducted smFRET analysis on a preQ₁-III riboswitch construct harboring fluorophores that report on helix P5 formation (Fig. 6A and Fig. S4C). In buffer containing Mg²⁺ at a near-physiological concentration, ~90% of riboswitches showed single-step photobleaching, consistent with the majority of molecules being monomeric under the low-concentration

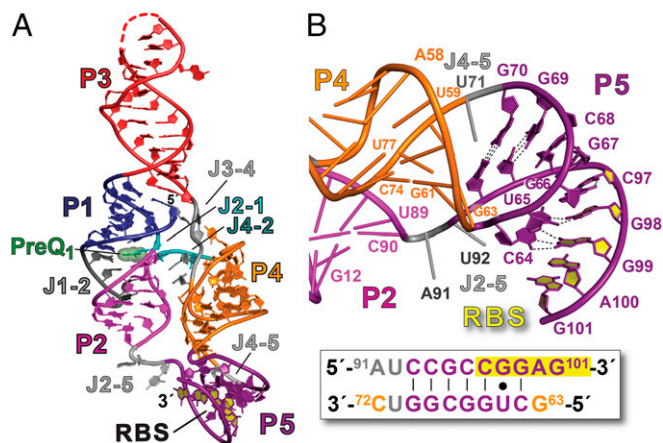


Fig. 5. Model of the preQ₁-III riboswitch showing intramolecular base pairing of the RBS in helix P5. (A) Cartoon diagram of a representative all-atom computational model demonstrating the feasibility of loop P4 engagement in an H-type pseudoknot that sequesters a portion of the RBS within helix P5, consistent with a “gene off” conformation. (B) Close-up view of P5 showing explicit base pairs between the anti-RBS of the P4 loop and the 3′ RBS, representing the “docked” state. The view is rotated -90° about the z axis, and $+45^\circ$ about the x axis relative to A. (Inset) The model accounts for the proposed P5 secondary structure from bioinformatic analysis (23). Base-paired nucleotides of P5 are $>93\%$ conserved. Unpaired base 71 of J4-5 is present in only 75% of sequences as any base, and unpaired nucleotides 91 and 92 of J2-5 indicate a 75% preference for purine followed by any base in 95% of sequences.

conditions of smFRET (Fig. 6B and Fig. S6A–C). Importantly, the monomeric state is compatible with expectations for folding and gene regulation in an intracellular environment, which is reflected by our computational model (Fig. 5). The FRET his-

togram of the monomeric population in the absence of preQ₁ showed a two-state distribution with a major (92%) ~ 0.55 mid-FRET state, and a minor (8%) ~ 0.89 high-FRET state (Fig. 6C and Fig. S7A–C). Under these conditions, a large fraction of the smFRET traces remained static in the mid-FRET state before photobleaching, but a smaller fraction was dynamic with multiple transitions between the two states (Fig. 6B, Top, and Fig. S6A). In a transition occupancy density plot (TODP), $\sim 32\%$ of all molecules showed dynamics (Fig. 6D, Top). This analysis demonstrates that the preQ₁-III riboswitch samples compactly folded P5 conformations in the absence of ligand, similar to preQ₁-I and other riboswitch classes (11, 35). As little as 25 nM preQ₁ increased the fraction of dynamic traces to $\sim 61\%$ with a further shift to $\sim 69\%$ at saturating 1 μM preQ₁ (Fig. 6B and D and Fig. S6B and C). Consistent with the small fraction of molecules occupying the transient high-FRET state at any given time, the addition of more ligand led to only a modestly larger contribution of the high-FRET state to the population histogram (14%; Fig. 6C). Though small, this increase in the high-FRET state was consistently reproducible in multiple experiments (Fig. S7A–C) and is supported by difference histogram analyses, which show decreases in the mid-FRET state and concomitant increases in the high-FRET population with added preQ₁ (Fig. S7D–F).

We then examined the effect of blocking P5 formation in the context of the wild-type *Fpr* preQ₁-III riboswitch using an 11-nt DNA strand complementary to the riboswitch 3′ terminus (Fig. S4C, Inset, and SI Methods). This anti-P5 competitor resulted in complete loss of the high-FRET state and rendered almost all molecules static in a ~ 0.4 mid-FRET state, both in the absence and presence of 1 μM preQ₁ (Fig. S8A–F). This finding further establishes that the high-FRET state corresponds to the P5 docked conformation wherein the RBS is sequestered. The lower mid-FRET value of ~ 0.4 compared with the ~ 0.55 value in the absence of DNA oligonucleotide suggests a small increase in

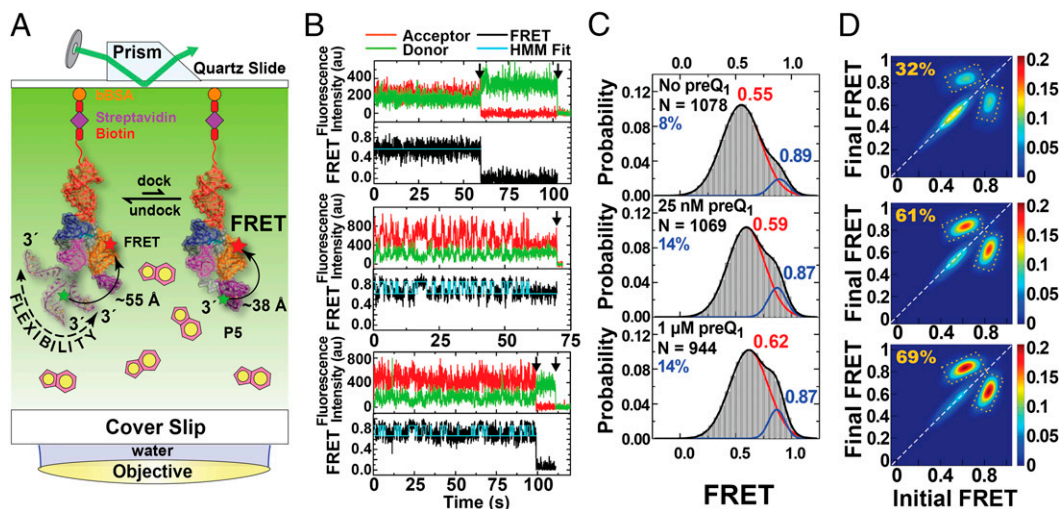


Fig. 6. smFRET analysis of the preQ₁-III riboswitch revealing the ligand dependence of dynamic RBS sequestration via P5 helix formation. (A) Schematic of the prism-based TIRF microscopy setup used to probe docking of helix P5 of the preQ₁-III riboswitch by smFRET. Position U77 is labeled with Cy5 (red star); the 3′ terminus is labeled with Dy547 (green star). The mid-FRET distance of ~ 55 Å corresponds to the length of the flexible self-avoiding polymer extending from position A91 to G101 (i.e., ~ 26.0 Å) (54) added to the C90–U77 distance from the computational model (Fig. 5). In this conformation, helix P5 is not formed or undocked. The high-FRET state is consistent with the ~ 38 Å distance between U77 and G101, observed in the preponderance of riboswitch models (Fig. S5F and G); in this conformation, helix P5 is formed as a double-stranded RNA duplex or docked. As a basis for comparison, the intramolecular U77–G101 distance in the crystal structure is 66 Å. (B) Representative smFRET traces for each condition in the presence of no preQ₁ (Top), 25 nM preQ₁ (Middle), and 1 μM preQ₁ (Bottom). Green, Dy547 intensity; red, Cy5 intensity; black, FRET efficiency; cyan, hidden Markov model fit. (C) FRET efficiency histograms of the preQ₁-III riboswitch under the ligand concentrations in B. N indicates the number of molecules included in each histogram. Percentages in blue correspond to the high-FRET population. The mean FRET values are shown as fractional numbers in red and blue. (D) TODPs depicting heat-map contours corresponding to static, on-diagonal molecules and dynamic, off-diagonal molecules; here the fraction of static and dynamic molecules is shown for each condition in B. The percentage of dynamic molecules, represented by off-diagonal contours (dashed boxes), is indicated in gold.

separation between the fluorophores, as expected for a more rigid RNA–DNA duplex. Furthermore, addition of a small molecule known not to bind the preQ₁-III riboswitch (i.e., isoxanthopterin (IXP) or 2-aminapurine (2AP); Fig. S1 I and J and SI Methods) revealed little increase in either the high-FRET state or the fraction of dynamic molecules, by contrast to preQ₁ (Fig. S8 G–P), thereby demonstrating a highly specific response that occurs only with the cognate ligand.

At the molecular level, the mean values of 0.55 and 0.89 for the mid- and high-FRET states correspond to distances of ~52 and ~38 Å, respectively. The mid-FRET state is consistent with the distance of ~55 Å expected for an undocked P5 helix in which the RBS is solvent-exposed and flexible (Fig. 6A). The mean FRET value of this undocked state increased from 0.55 to 0.62 upon preQ₁ addition (Fig. 6C), signifying a small compaction in the presence of ligand. The high-FRET state agrees well with distances observed for the preQ₁-III riboswitch model in which P5 is docked (Fig. 5); specifically, the U77 to G101 distance that approximates the FRET pair was observed to be bimodal over 8 μs of MD simulations with maxima at ~37 and ~40 Å (Fig. S5 F and G). We also noted that in the absence of ligand, most traces displayed either static or dynamic behavior and switched rarely (<1%) between the two regimes (Fig. S8Q), which suggests that the two species interconvert slowly during our observation window (~5 min) before photobleaching. However, individual molecules were observed to switch in situ from the static to the dynamic regime upon preQ₁ addition (Fig. S8R), suggesting that ligand accelerates the transition into the dynamic, “active” conformation while the kinetics of dynamic molecules appeared unchanged. In the latter regard, the dynamic smFRET traces showed homogeneous kinetics that allowed us to calculate the rate constants of docking ($k_{\text{dock}} = 0.59 \pm 0.03 \text{ s}^{-1}$) and undocking ($k_{\text{undock}} = 1.10 \pm 0.06 \text{ s}^{-1}$) in the absence of preQ₁. Notably, the rate constants were not affected substantially by addition of 25 nM or 1 μM preQ₁ (Table 2). These relatively fast rate constants, and the diminutive size of the high-FRET population at equilibrium, provide a plausible explanation for the inability to observe preQ₁-dependent formation of the P5 helix by SHAPE (Fig. 4).

ITC analysis indicated that preQ₁ binds the class III riboswitch in the absence of Mg²⁺ (Table S1), a result that is corroborated by smFRET analysis in which Mg²⁺-free experiments produced histograms similar to those in the presence of Mg²⁺ (Fig. S9A). However, the absence of Mg²⁺ resulted in heterogeneous kinetics wherein the weighted-mean value of k_{dock} increased, and k_{undock} was practically unchanged upon preQ₁ addition (Table 2). These results suggest that the preQ₁-III riboswitch transiently samples a docked P5 conformation even in the absence of both Mg²⁺ and preQ₁ (Fig. S9 B and C). Notably, even though the addition of preQ₁ affects P5 docking in the absence of Mg²⁺, the fraction of dynamically docking P5 helices is unaltered (Fig. S9D). The lack of preQ₁ dependence and absence of Mg²⁺ diminish the likelihood that such dy-

namics are operative in gene control. Instead, our regulatory model is best framed within the context of near-physiological Mg²⁺ concentrations wherein the addition of preQ₁ does not alter docking and undocking rates (Table 2) but enhances the fraction of molecules competent to undergo dynamic P5 docking (Fig. 6D), thus leading to RBS sequestration within the 3'-terminal H-type pseudoknot (Fig. 5B).

Discussion

Here we report the crystal structure of a preQ₁-III riboswitch bound to its effector (Figs. 1C and 2), thereby establishing the fold of a new class of regulatory RNA. The riboswitch can be parsed structurally into an aptamer domain composed of an HL_{out}-type pseudoknot that has co-opted major-groove base triples for ligand recognition (Fig. 3), and a downstream, partially embedded H-type pseudoknot that sequesters the RBS (Fig. 5). Such structural organization is uncommon among riboswitches (7, 19) and has not been investigated to an appreciable extent in terms of structure–function relationships (35). As such, we established a functional framework for the preQ₁-III riboswitch that entails ligand-dependent folding in the presence of Mg²⁺ to promote a compact aptamer that is conducive to dynamic docking and undocking of the remotely positioned RBS (Fig. 6A). Frequent docking of the RBS would sequester the expression platform, leading to ligand-dependent *queT* gene control by translational attenuation. This paradigm differs from other riboswitches, such as preQ₁-II and SAM-II, because these molecules integrate RBS sequences directly into their aptamer domains upon ligand binding (8, 10, 12, 16, 18). Consequently, RBS docking within these riboswitches is characterized by prolonged high-FRET dwell times in the presence of Mg²⁺ and ligand (>2.2 s and ~3.5 s, respectively) with timescales limited most likely by fluorophore photobleaching (10, 16). By contrast, the preQ₁-III riboswitch displays dwell times of ~0.9 s for the RBS-docked state, and ~1.8 s for the undocked state (Fig. S6 D–F). This dynamic character differentiates the preQ₁-III riboswitch from other regulatory RNAs that appear to rely upon comparatively static conformational states to achieve RBS sequestration.

We then considered the molecular basis by which effector binding to the preQ₁-III aptamer leads to a larger population of riboswitches that dynamically sequester the remote RBS. Our results indicated that preQ₁ binding only marginally stabilizes P5 docking, which occurs entirely through an increasing fraction of molecules that dynamically access the high-FRET docked state, and is evident in our kinetic analysis wherein no substantive rate changes occurred in k_{dock} (~0.6 s⁻¹) or k_{undock} (~1.1 s⁻¹) under conditions containing Mg²⁺ and preQ₁ vs. those with Mg²⁺ and no ligand (Table 2). These observations are consistent with a ligand-dependent aptamer conformation that reorients preformed helix P4 acutely relative to the P2–P1–P3 coaxial stack. Such positioning would predispose helix P5 to dock, thus completing the H-type pseudoknot with concomitant RBS burial.

Table 2. PreQ₁-III riboswitch P5 kinetics based on smFRET

Conditions		$k_{\text{dock}}, \text{s}^{-1}$			$k_{\text{undock}}, \text{s}^{-1}$		
Mg ²⁺ , mM	PreQ ₁ , nM	Fast	Slow	Weighted mean	Fast	Slow	Weighted mean
1.0*	None	n/a [†]	n/a	0.59 ± 0.03	n/a	n/a	1.10 ± 0.06
1.0	25	n/a	n/a	0.60 ± 0.01	n/a	n/a	1.13 ± 0.06
1.0	1,000	n/a	n/a	0.55 ± 0.01	n/a	n/a	1.08 ± 0.03
None [‡]	None	0.38 ± 0.01	0.05 ± 0.001	0.09	0.79 ± 0.01	0.12 ± 0.001	0.27
None	25	0.50 ± 0.01	0.06 ± 0.001	0.16	0.92 ± 0.02	0.12 ± 0.002	0.23

*The errors reported for the kinetics in 1.0 mM Mg²⁺ are SDs from three independent experiments.

[†]n/a, not applicable, because the rate was fit with a single exponential.

[‡]For conditions with no Mg²⁺, the SEs are derived from the quality of fits to a double-exponential function.

Our computational model demonstrates the feasibility and stability of this relatively compact fold (Fig. 5 and Fig. S5 D and E), which requires preQ₁ binding for full efficacy (Fig. 6D and Fig. S8).

Coupling of preQ₁ binding within the HL_{out}-type pseudoknot aptamer to distal RBS sequestration within the H-type pseudoknot depends on inclined A-minor base A52 of J3-4 and base A84 of J4-2, which are 75% and 97% conserved (23). ITC confirmed that both adenines affect preQ₁ binding (Fig. 2B and Table S1), although neither base hydrogen bonds directly to the ligand. SHAPE analysis revealed greater backbone stability of these nucleotides in the presence of preQ₁, which is corroborated by the crystal structure (Fig. 4 C and D). Specifically, preQ₁ engages in a T-shaped π -stacking interaction with A84, which simultaneously forms a cross-strand stacking interaction with A52 (Fig. 7A). Importantly, the stacking of A84 upon A52 abuts

a network of continuously stacked bases in helix P4 that begins at A53 and culminates in the anti-RBS sequence (Fig. 7A). This stacking network is maintained in the computational model wherein helix P5 is docked by pairing of the anti-RBS and RBS sequences, which requires helix P4 repositioning (Fig. 7B). In this manner, preQ₁ binding establishes a continuous stacking network that predisposes P4 to reorient acutely toward the P1–P2 coaxial stack, favoring P5 docking and RBS sequestration.

Although the broader role of inclined A-minor bases in the context of H- and HL_{out}-type pseudoknots is to stabilize a 5'-terminal stem (7), the preQ₁-II riboswitch provides a precedent for the use of such adenine bases in mediating base stacking between a ligand and a nearby orthogonal stem-loop (Fig. 7C). Specifically, preQ₁ binding to the class II riboswitch alters P4 helical dynamics and its proximity to the orthogonally oriented aptamer domain (12, 16). Like the preQ₁-III riboswitch, ITC analysis of preQ₁-II A-minor adenines verified the importance of these bases in preQ₁ binding, although larger $\Delta\Delta G$ values were observed upon mutagenesis indicative of greater losses in ligand binding (12). Nonetheless, there is notable structural homology between the inclined A-minor adenines of the preQ₁-II and preQ₁-III riboswitches (Fig. 7 A and B vs. Fig. 7C) that lends support for the mode by which preQ₁ binding to the preQ₁-III aptamer can influence the orientation of helix P4 in a manner that favors formation of distal helix P5 and concurrent RBS sequestration. Conversely, ligand deficiency in the preQ₁-III aptamer domain destabilizes helices P1 and P2, resulting in increased flexibility of the inclined A-minor bases (Fig. 4). Thus, although a fraction of the riboswitch population can dynamically sequester the RBS in the absence of ligand, translational control by the preQ₁-III riboswitch requires a folded aptamer and preQ₁ binding for greatest efficacy (Fig. 6D and Fig. S8).

Overall, our results provide a molecular-level framework to understand how effector binding within the preQ₁-III riboswitch aptamer influences the conformation of a distal expression platform. In this context, the dynamic character of the RBS is unusual compared with other riboswitches, and our work demonstrates how a nonintegrated expression platform can achieve ligand-dependent translational attenuation without burial in the aptamer core. This paradigm is likely applicable to other riboswitches, especially those with bipartite structural organization, thus expanding the known repertoire of translational attenuation strategies.

Methods

Riboswitch Production and Isothermal Titration Calorimetry. *Faecalibacterium prausnitzii* (*Fpr*) preQ₁-III riboswitches and mutants thereof (Fig. 1B and Table S1) were generated by in vitro transcription and purified by denaturing PAGE (36). The 74 *env* sequences (Fig. S4A) were produced by chemical synthesis (GE Life Sciences) and HPLC purified (37); preQ₁ was prepared as described (18). Lyophilized RNA was suspended in a folding buffer comprising 0.050 M Na-Hepes (pH 7.0) containing 0.10 M NaCl. The *Fpr* RNA was heated to 65 °C for 5 min followed by addition of 0.006 M MgCl₂ or 0.0005 M EDTA before slow cooling. The 74 *env* RNA was folded by heating each strand at 70 °C, mixing the strands, and incubating at 37 °C for 2 min before the addition of Mg²⁺. Samples were then incubated at 37 °C for 20 min followed by flash cooling on ice. ITC measurements were conducted using a VP-ITC calorimeter (MicroCal, Inc.) as described (38) in which the folding buffer above included 0.006 M MgCl₂ or 0.0005 M EDTA to produce ITC buffer. Each sample (Fig. S1) was dialyzed at 4 °C overnight against 4 L of ITC buffer. RNA was diluted with dialysis buffer to 3.1–3.3 μ M for wild-type *Fpr*, 3.2–7.8 μ M for the A52G and A84G *Fpr* mutants, 10.5–15.7 μ M for the C7U and U17C *Fpr* mutants, 2.4–3.6 μ M for 74 *env*, and 1.8 μ M for 74 *env*-s2430–43. PreQ₁ was dissolved in dialysis buffer at concentrations ~10-fold higher than RNA. Thermograms were analyzed with Origin 7.0 (MicroCal) using a 1:1 binding model. Average thermodynamic parameters and representative thermograms with curve fits are provided (Table S1 and Fig. S1). See *SI Methods* for details of the IXP and 2AP control experiments.

Riboswitch Crystallization and X-ray Data Collection. PreQ₁-III riboswitch RNA (Fig. 1B) was dissolved to 0.16 mM in 0.010 M Na-cacodylate (pH 7.0). RNA

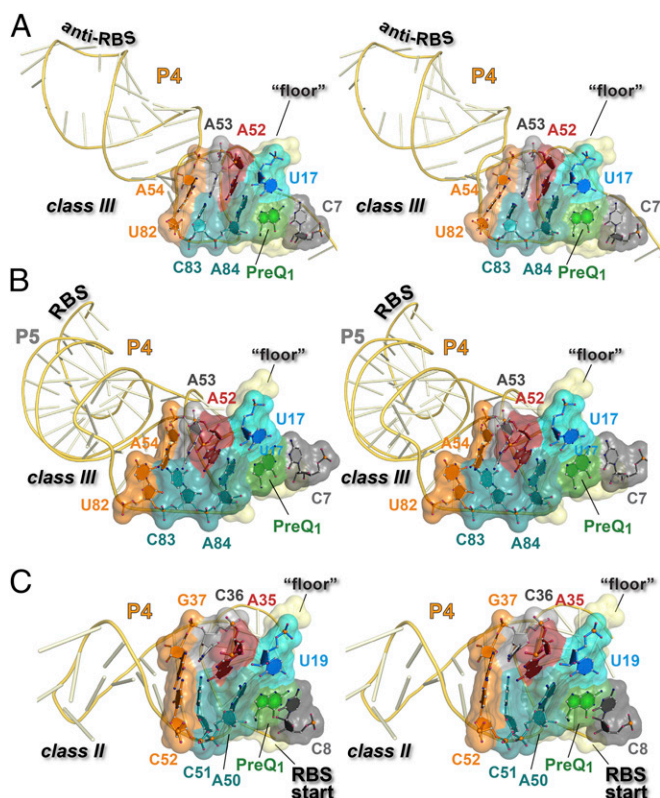


Fig. 7. Stereo diagrams depicting inclined A-minor bases of the preQ₁-II and preQ₁-III riboswitches mediating stacking interactions between the ligand and a nearby helix. (A) The preQ₁-III riboswitch crystal structure depicting nucleotides that compose the binding pocket and flank the ligand (rendered as transparent surfaces covering ball-and-stick models); helix P4 is drawn as a ribbon with nucleotides depicted as sticks. The pyrrole ring of preQ₁ forms an edge-to-face interaction with A-minor base A84 that is integral to formation of the binding pocket. On its opposite face, A84 stacks upon A52, forming a cross-strand interaction. A52 also stacks against neighboring purine A53, establishing a continuous base stack through helix P4 that culminates in the anti-RBS loop. In this manner, preQ₁ occupancy within the binding pocket influences the orientation of P4. The view is similar to Fig. 2B. (B) Representative computational model of the preQ₁-III riboswitch bound to preQ₁ as described in A. The inclined A-minor interactions of the crystal structure (Fig. 2B) are preserved in the model, and base stacking is still continuous from A84 to the anti-RBS, despite formation of the P5 helix that sequesters the RBS. (C) Analogous view of the preQ₁-II riboswitch (PDB ID code 2MIY) (12) illustrating preQ₁ packing against structurally homologous inclined A-minor bases A50 and A35. Like the preQ₁-III riboswitch, these bases form a continuous stacking interaction that influences the conformation of helix P4. Here, the pocket floor contains the first base of the RBS (yellow) located directly beneath preQ₁.

was folded by heating to 65 °C for 3 min followed by addition of 0.006 M MgCl₂ and 0.32 mM preQ₁; subsequently, the RNA was heated to 65 °C for 5 min, followed by slow cooling and 0.2- μ m filtration. Crystals were prepared by the hanging-drop vapor-diffusion method in which 1.6–2.0 μ L of folded RNA was mixed with an equal volume of well solution, followed by equilibration over 1 mL of well solution at 20 °C. Crystals grew as hexagonal rods within 24 h and achieved a maximum size of 0.2 \times 0.05 \times 0.05 mm within a week. See *SI Methods* for crystallization solutions. All crystals were flash-frozen by washing in well solution supplemented with 0.32 mM preQ₁, then plunging into N₂(l). X-ray diffraction data for phasing were recorded at the Stanford Synchrotron Radiation Lightsources (SSRL) beamline 7-1. Phasing module (PM) data were reduced with HKL2000 software (39). High-resolution data were recorded at SSRL beamline 11-1 and reduced with XDS/XSCALE (40) (Table 1).

Phase Determination, Refinement, and Analysis. Experimental phases were obtained by single isomorphous replacement with anomalous scattering (SIRAS) to 3.0 Å resolution. Subsequently, the resolution was extended to 2.75-Å resolution with refinement to reasonable R_{factors} and geometry (Table 1). Details are available in *SI Methods*.

Chemical Modification by Selective 2'-Hydroxyl Acylation Analyzed by Primer Extension. The ligand-dependent acylation of the *Fpr* preQ₁-III riboswitch was probed by SHAPE (41) (Fig. 4 and Fig. S4B); nicotinic acid imidazole (NAI) was synthesized as described (42). Purified RNA from *in vitro* transcription (36) was heated in metal-free water for 2 min at 95 °C, then flash-cooled on ice. A 3 \times SHAPE buffer [0.333 M Hepes (pH 8.0), 0.02 M MgCl₂, 0.333 M NaCl] was added and the RNA was equilibrated at 37 °C for 10 min. A total of 1 μ L of preQ₁ stock (1 M in 1 \times PBS) was added to the RNA. The RNA was incubated at 37 °C for 15 min. To this mixture, 1 μ L of 10 \times NAI stock in DMSO (+), or DMSO alone (–) (Fig. 4 A and B), was added to a final concentration of 0.06 M. The NAI reaction proceeded for 15 min followed by one extraction with acid phenol:chloroform (pH 4.5 \pm 0.2) and two with chloroform. RNA was precipitated with 40 μ L of 3 M sodium acetate (pH 5.2) containing 1 μ L of glycogen (20 μ g μ L⁻¹). Pellets were washed twice with 70% ethanol and suspended in 10 μ L RNase-free water. Extension using ³²P-labeled primer and data analysis were as described (41, 42).

Riboswitch Modeling and MD Simulations. To evaluate the feasibility of P5 base pairing, a steered MD simulation was performed starting from the *Fpr* crystal structure (Fig. 1C). The P4 loop (nucleotides 64–70) was moved toward nucleotides 93–99 using distance restraints with three force-constant steps applied over a total time of 10 ns. The equilibrium distance between the heavy atom of the hydrogen bond acceptor to the hydrogen atom of the donor was set to 2.5 Å. First, the distance restraint force constant was ramped from 0 to 5 kcal (mol \times Å²)⁻¹ in 100 ps, followed by an interval of constant force, and then a ramp from 5 to 0 kcal (mol \times Å²)⁻¹ in the last 100 ps. The restraints were harmonic to 15 Å, and then the potential became flat. Each hydrogen bond of a canonical base pair in P5 was restrained. A model was selected manually from 10 pulling simulations that exhibited features consistent with the “modeling restraints” derived from the crystal structure (Fig. 1C), ITC (Fig. 2B), SHAPE (Fig. 4C), as well as prior *in-line* probing and bioinformatic analyses (23). This model was then subjected to two-stage minimization. First, the riboswitch was fixed spatially with a restraint force of 500 kcal (mol \times Å²)⁻¹, and solvent and counterions were

energy minimized for 5,000 steps. Next, solvent and RNA were minimized for 5,000 steps. Each minimization had 2,500 steepest descent steps, followed by 2,500 conjugate gradient steps. The final system was subjected to 100 ps of heating from 0 to 300 K in the canonical ensemble [i.e., the NVT ensemble comprising a constant number of particles (N), volume (V), and temperature (T)] by holding the RNA in space with a harmonic potential of 10 kcal (mol \times Å²)⁻¹. Finally, 100 ps of isothermal-isobaric ensemble [i.e., the NPT ensemble comprising a constant N, pressure (P), and T] simulation was performed to equilibrate at 300 K; a Langevin thermostat was used for temperature control with a collision frequency of 1,000 ps⁻¹. The particle-mesh Ewald (43, 44) method was used to calculate long-range electrostatics with a 10-Å cutoff for the direct space sum. Bonds involving hydrogen were restrained by the program SHAKE (45). Additional details are provided in *SI Methods*.

Single-Molecule FRET Analysis. The *Fpr* preQ₁-III riboswitch was produced by chemical synthesis (GE Life Sciences) from two RNA strands (Fig. S4C). The feasibility of producing a functional split riboswitch was demonstrated by ITC analysis of the 74 *env* preQ₁-III riboswitch, which yielded an apparent K_D of 10.1 \pm 2.5 nM (Table S1 and Figs. S1B and S4A), indicating high-affinity preQ₁ binding. Extension of the 5'-RNA smFRET strand allowed hybridization to a biotinylated DNA tether (IDT, Inc.). The RNA strand harboring the RBS included 5-amino-allyl-U77 and Dy547 at the 3' terminus. A Cy5 label (GE Healthcare) was added as described (46), and both RNA strands were PAGE-purified and desalted (36). To fold the RNA, 1 μ M of each strand was combined and annealed at 70 °C for 3 min in 0.050 M Hepes–KOH (pH 7.0). KCl was added to a concentration of 0.1 M with additional heating at 70 °C for 2 min followed by 5-min incubation at 37 °C. The RNA was cooled to 23 °C for 10 min. smFRET experiments were performed using a prism-based total internal reflection fluorescence (TIRF) microscopy setup (Fig. 6A) (11, 47). Briefly, quartz slides containing microfluidic channels were coated with biotinylated BSA followed by streptavidin treatment. Unbound protein was washed away by 1 \times smFRET buffer [0.050 M Hepes–KOH (pH 7.0), 0.1 M KCl, with or without 0.001 M Mg²⁺]. Immobilization of 10–25 μ M of folded riboswitch was achieved using the biotin–streptavidin interaction. Unbound molecules were washed away with 1 \times smFRET buffer. An oxygen scavenging system (OSS) containing 5 mM protocatechuic acid, 50 nM protocatechuate 3,4-dioxygenase, and 2 mM Trolox in smFRET buffer was used to prolong fluorophore longevity and reduce photoblinking (11). Molecules were imaged by an intensified-CCD camera (i-PentaMAX; Princeton Instruments) at a time resolution of \sim 60 ms in the absence or presence of various preQ₁ concentrations. Dy547 was excited directly using a 532-nm laser, and emission intensities from both Dy547 (donor, I_D) and Cy5 (acceptor, I_A) were recorded simultaneously, and used to calculate the FRET ratio as $I_A/(I_A + I_D)$ after background correction. The raw FRET movies were processed using IDL (Research Systems) to extract time traces of individual molecules, and analyzed further by custom MATLAB (MathWorks) scripts. See *SI Methods* for further details.

ACKNOWLEDGMENTS. We thank J. Jenkins, S. Bellaousov, E. Salsi, D. Ermolenko, and C. Kielkopf for helpful analysis and discussion, and C. Brooks for editing assistance. This research was funded by NIH Grants GM076485 (to D.H.M.), GM062357 (to N.G.W.), and RR026501 and GM063162 (to J.E.V.). Portions of this work were conducted at SSRL, funded by NIH Grants GM103393 and RR001209, and the Department of Energy.

- Serganov A, Nudler E (2013) A decade of riboswitches. *Cell* 152(1-2):17–24.
- Roth A, Breaker RR (2009) The structural and functional diversity of metabolite-binding riboswitches. *Annu Rev Biochem* 78:305–334.
- Sudarsan N, Cohen-Chalimish S, Nakamura S, Emilsson GM, Breaker RR (2005) Thiamine pyrophosphate riboswitches are targets for the antimicrobial compound pyrithiamine. *Chem Biol* 12(12):1325–1335.
- Blount KF, Wang JX, Lim J, Sudarsan N, Breaker RR (2007) Antibacterial lysine analogs that target lysine riboswitches. *Nat Chem Biol* 3(1):44–49.
- Lee ER, Blount KF, Breaker RR (2009) Roseoflavin is a natural antibacterial compound that binds to FMN riboswitches and regulates gene expression. *RNA Biol* 6(2):187–194.
- Breaker RR (2012) Riboswitches and the RNA world. *Cold Spring Harb Perspect Biol* 4(2):a003566.
- Peselis A, Serganov A (2014) Structure and function of pseudoknots involved in gene expression control. *Wiley Interdiscip Rev RNA* 5(6):803–822.
- Gilbert SD, Rambo RP, Van Tynne D, Batey RT (2008) Structure of the SAM-II riboswitch bound to S-adenosylmethionine. *Nat Struct Mol Biol* 15(2):177–182.
- Spitale RC, Torelli AT, Krucinska J, Bandarian V, Wedekind JE (2009) The structural basis for recognition of the PreQ₀ metabolite by an unusually small riboswitch aptamer domain. *J Biol Chem* 284(17):11012–11016.
- Haller A, Rieder U, Aigner M, Blanchard SC, Micura R (2011) Conformational capture of the SAM-II riboswitch. *Nat Chem Biol* 7(6):393–400.
- Suddala KC, et al. (2013) Single transcriptional and translational preQ₁ riboswitches adopt similar pre-folded ensembles that follow distinct folding pathways into the same ligand-bound structure. *Nucleic Acids Res* 41(22):10462–10475.
- Kang M, Eichhorn CD, Feigon J (2014) Structural determinants for ligand capture by a class II preQ₁ riboswitch. *Proc Natl Acad Sci USA* 111(6):E663–E671.
- Jenkins JL, Krucinska J, McCarty RM, Bandarian V, Wedekind JE (2011) Comparison of a preQ₁ riboswitch aptamer in metabolite-bound and free states with implications for gene regulation. *J Biol Chem* 286(28):24626–24637.
- Kang M, Peterson R, Feigon J (2009) Structural Insights into riboswitch control of the biosynthesis of queuosine, a modified nucleotide found in the anticodon of tRNA. *Mol Cell* 33(6):784–790.
- Klein DJ, Edwards TE, Ferré-D'Amaré AR (2009) Cocystal structure of a class I preQ₁ riboswitch reveals a pseudoknot recognizing an essential hypermodified nucleobase. *Nat Struct Mol Biol* 16(3):343–344.
- Soulière MF, et al. (2013) Tuning a riboswitch response through structural extension of a pseudoknot. *Proc Natl Acad Sci USA* 110(35):E3256–E3264.
- Ren A, Rajashankar KR, Patel DJ (2012) Fluoride ion encapsulation by Mg²⁺ ions and phosphates in a fluoride riboswitch. *Nature* 486(7401):85–89.

18. Liberman JA, Salim M, Krucinska J, Wedekind JE (2013) Structure of a class II preQ₁ riboswitch reveals ligand recognition by a new fold. *Nat Chem Biol* 9(6):353–355.
19. Trausch JJ, et al. (2014) Structural basis for diversity in the SAM clan of riboswitches. *Proc Natl Acad Sci USA* 111(18):6624–6629.
20. Gao A, Serganov A (2014) Structural insights into recognition of c-di-AMP by the ydaO riboswitch. *Nat Chem Biol* 10(9):787–792.
21. Jones CP, Ferré-D'Amaré AR (2014) Crystal structure of a c-di-AMP riboswitch reveals an internally pseudo-dimeric RNA. *EMBO J* 33(22):2692–2703.
22. Ren A, Patel DJ (2014) c-di-AMP binds the ydaO riboswitch in two pseudo-symmetry-related pockets. *Nat Chem Biol* 10(9):780–786.
23. McCown PJ, Liang JJ, Weinberg Z, Breaker RR (2014) Structural, functional, and taxonomic diversity of three preQ₁ riboswitch classes. *Chem Biol* 21(7):880–889.
24. Noguchi S, Nishimura Y, Hirota Y, Nishimura S (1982) Isolation and characterization of an *Escherichia coli* mutant lacking tRNA-guanine transglycosylase. Function and biosynthesis of queuosine in tRNA. *J Biol Chem* 257(11):6544–6550.
25. Harada F, Nishimura S (1972) Possible anticodon sequences of tRNA His, tRNA Asn, and tRNA Asp from *Escherichia coli* B. Universal presence of nucleoside Q in the first position of the anticodons of these transfer ribonucleic acids. *Biochemistry* 11(2):301–308.
26. Bienz M, Kubli E (1981) Wild-type transfer-RNA G^{Tyr} reads the TMV RNA stop codon, but Q-base-modified transfer-RNA G^{Tyr} does not. *Nature* 294(5837):188–190.
27. Meier F, Suter B, Grosjean H, Keith G, Kubli E (1985) Queuosine modification of the wobble base in tRNA^{His} influences 'in vivo' decoding properties. *EMBO J* 4(3):823–827.
28. Urbanavičius J, Qian Q, Durand JM, Hagervall TG, Björk GR (2001) Improvement of reading frame maintenance is a common function for several tRNA modifications. *EMBO J* 20(17):4863–4873.
29. Katze JR, Basile B, McCloskey JA (1982) Queuine, a modified base incorporated posttranscriptionally into eukaryotic transfer RNA: Wide distribution in nature. *Science* 216(4541):55–56.
30. Rakovich T, et al. (2011) Queuosine deficiency in eukaryotes compromises tyrosine production through increased tetrahydrobiopterin oxidation. *J Biol Chem* 286(22):19354–19363.
31. Durand JM, et al. (1994) vacC, a virulence-associated chromosomal locus of *Shigella flexneri*, is homologous to tgt, a gene encoding tRNA-guanine transglycosylase (Tgt) of *Escherichia coli* K-12. *J Bacteriol* 176(15):4627–4634.
32. Meyer MM, Roth A, Chervin SM, Garcia GA, Breaker RR (2008) Confirmation of a second natural preQ₁ aptamer class in Streptococcaceae bacteria. *RNA* 14(4):685–695.
33. Roth A, et al. (2007) A riboswitch selective for the queuosine precursor preQ₁ contains an unusually small aptamer domain. *Nat Struct Mol Biol* 14(4):308–317.
34. Smith KD, Shanahan CA, Moore EL, Simon AC, Strobel SA (2011) Structural basis of differential ligand recognition by two classes of bis-(3'-5')-cyclic dimeric guanosine monophosphate-binding riboswitches. *Proc Natl Acad Sci USA* 108(19):7757–7762.
35. Savinov A, Perez CF, Block SM (2014) Single-molecule studies of riboswitch folding. *Biochim Biophys Acta* 1839(10):1030–1045.
36. Lippa GM, et al. (2012) Crystallographic analysis of small ribozymes and riboswitches. *Methods Mol Biol* 848:159–184.
37. Wedekind JE, McKay DB (2000) Purification, crystallization, and X-ray diffraction analysis of small ribozymes. *Methods Enzymol* 317:149–168.
38. Liberman JA, Bogue JT, Jenkins JL, Salim M, Wedekind JE (2014) ITC analysis of ligand binding to preQ₁ riboswitches. *Methods Enzymol* 549:435–450.
39. Otwinowski Z, Minor W (1997) Processing of X-ray diffraction data collected in oscillation mode. *Methods Enzymol* 276:307–326.
40. Kabsch W (2010) Integration, scaling, space-group assignment and post-refinement. *Acta Crystallogr D Biol Crystallogr* 66(Pt 2):133–144.
41. Wilkinson KA, Merino EJ, Weeks KM (2006) Selective 2'-hydroxyl acylation analyzed by primer extension (SHAPE): Quantitative RNA structure analysis at single nucleotide resolution. *Nat Protoc* 1(3):1610–1616.
42. Spitale RC, et al. (2013) RNA SHAPE analysis in living cells. *Nat Chem Biol* 9(1):18–20.
43. Toukhami A, Sagui C, Board J, Darden T (2000) Efficient particle-mesh Ewald based approach to fixed and induced dipolar interactions. *J Chem Phys* 113:10913–10927.
44. Sagui C, Pedersen LG, Darden TA (2004) Towards an accurate representation of electrostatics in classical force fields: Efficient implementation of multipolar interactions in biomolecular simulations. *J Chem Phys* 120(1):73–87.
45. Miyamoto S, Kollman PA (1992) Settle: An analytical version of the SHAKE and RATTLE algorithm for rigid water models. *J Comput Chem* 13:952–962.
46. Akiyama BM, Stone MD (2009) Assembly of complex RNAs by splinted ligation. *Methods Enzymol* 469:27–46.
47. Suddala KC, Walter NG (2014) Riboswitch structure and dynamics by smFRET microscopy. *Methods Enzymol* 549:343–373.
48. Soltis SM, et al. (2008) New paradigm for macromolecular crystallography experiments at SSRL: Automated crystal screening and remote data collection. *Acta Crystallogr D Biol Crystallogr* 64(Pt 12):1210–1221.
49. Weiss MS (2001) Global indicators of X-ray data quality. *J Appl Cryst* 34:130–135.
50. Karpplus PA, Diederichs K (2012) Linking crystallographic model and data quality. *Science* 336(6084):1030–1033.
51. Adams PD, et al. (2010) PHENIX: A comprehensive Python-based system for macromolecular structure solution. *Acta Crystallogr D Biol Crystallogr* 66(Pt 2):213–221.
52. McCarty RM, Bandarian V (2012) Biosynthesis of pyrrolopyrimidines. *Bioorg Chem* 43:15–25.
53. Keel AY, Rambo RP, Batey RT, Kieft JS (2007) A general strategy to solve the phase problem in RNA crystallography. *Structure* 15(7):761–772.
54. Aalberts DP, Nandagopal N (2010) A two-length-scale polymer theory for RNA loop free energies and helix stacking. *RNA* 16(7):1350–1355.
55. Emsley P, Cowtan K (2004) Coot: Model-building tools for molecular graphics. *Acta Crystallogr D Biol Crystallogr* 60(Pt 12 Pt 1):2126–2132.
56. Cheatham TE, 3rd, Cieplak P, Kollman PA (1999) A modified version of the Cornell et al. force field with improved sugar pucker phases and helical repeat. *J Biomol Struct Dyn* 16(4):845–862.
57. Pérez A, et al. (2007) Refinement of the AMBER force field for nucleic acids: Improving the description of alpha/gamma conformers. *Biophys J* 92(11):3817–3829.
58. Zgarbová M, et al. (2011) Refinement of the Cornell et al. nucleic acids force field based on reference quantum chemical calculations of glycosidic torsion profiles. *J Chem Theory Comput* 7(9):2886–2902.
59. Aytenuf AH, Spasic A, Seetin MG, Serafini J, Mathews DH (2014) Modified AMBER force field correctly models the conformational preference for tandem GA pairs in RNA. *J Chem Theory Comput* 10(3):1292–1301.
60. Jorgensen WL, Chandrasekhar J, Madura JD, Impey RW, Klein ML (1983) Comparison of simple potential functions for simulating liquid water. *J Chem Phys* 79(2):926–935.
61. Joung IS, Cheatham TE, 3rd (2008) Determination of alkali and halide monovalent ion parameters for use in explicitly solvated biomolecular simulations. *J Phys Chem B* 112(30):9020–9041.
62. Joung IS, Cheatham TE, 3rd (2009) Molecular dynamics simulations of the dynamic and energetic properties of alkali and halide ions using water-model-specific ion parameters. *J Phys Chem B* 113(40):13279–13290.
63. Case DA, et al. (2014) AMBER (University of California, San Francisco).
64. Bayly CI, Cieplak P, Cornell WD, Kollman PA (1993) A well-behaved electrostatic potential based method using charge restraints for deriving atomic charges: The RESP model. *J Phys Chem* 97(40):10269–10280.
65. Dupradeau FY, et al. (2010) The R.E.D. tools: Advances in RESP and ESP charge derivation and force field library building. *Phys Chem Chem Phys* 12(28):7821–7839.
66. Vanqualef E, et al. (2011) R.E.D. Server: A web service for deriving RESP and ESP charges and building force field libraries for new molecules and molecular fragments. *Nucleic Acids Res* 39(Web Server issue):W511–7.
67. Case DA, et al. (2005) The Amber biomolecular simulation programs. *J Comput Chem* 26(16):1668–1688.
68. Qin F (2004) Restoration of single-channel currents using the segmental k-means method based on hidden Markov modeling. *Biophys J* 86(3):1488–1501.
69. Blanco M, Walter NG (2010) Analysis of complex single-molecule FRET time trajectories. *Methods Enzymol* 472:153–178.
70. Han K, Byun Y (2003) PSEUDOVIEWER2: Visualization of RNA pseudoknots of any type. *Nucleic Acids Res* 31(13):3432–3440.
71. Terwilliger TC, et al. (2008) Iterative-build OMIT maps: Map improvement by iterative model building and refinement without model bias. *Acta Crystallogr D Biol Crystallogr* 64(Pt 5):515–524.

Supporting Information

Liberman et al. 10.1073/pnas.1503955112

SI Methods

Riboswitch ITC Control Experiments. Control experiments with nonbinding compounds used IXP (Carbosynth Ltd.) and 2AP (TCI America). For control experiments, 33 μM IXP or 150 μM 2AP was titrated into 3.2 μM wild-type *Fpr*. Representative thermograms and chemical structures are provided (Fig. S1 I and J).

Riboswitch Crystallization Solutions. The well solutions of hanging-drop experiments were composed of the following conditions. To prepare a “native” crystal of the PM construct with a G•U pair (53) (Fig. 1B, *Inset*), 74.5% Tacsimate (pH 7.0; Hampton Research), was combined with 0.050 M Mops (pH 7.0), 0.020 M $\text{Co}(\text{NH}_3)_6\text{Cl}_3$, and 0.001 M spermine•HCl. The well solution used to prepare a heavy atom-derivatized PM crystal contained 1.9 M Na-malonate (pH 7.0; Hampton Research), 0.20 M CsCl, 0.050 M Na-Mops (pH 7.0), 0.050 M $\text{Mg}(\text{C}_2\text{H}_3\text{O}_2)_2$, and 0.001 M spermine•HCl. Crystals of the wild-type sequence (Fig. 1B) used for high-resolution refinement were prepared from a well solution of 85% Tacsimate (pH 7.0), 0.010 M $\text{Mg}(\text{C}_2\text{H}_3\text{O}_2)_2$, 0.006 M $\text{Co}(\text{NH}_3)_6\text{Cl}_3$, and 0.001 M spermine•HCl.

Phase Determination, Refinement, and Analysis. The phase problem was solved by SIRAS to 3.0 Å resolution. To prepare a heavy-atom derivative, a crystal of the PM construct was cocrystallized with Cs^+ , and yielded a dataset with measurable anomalous diffraction to 4.45 Å using Phenix.xtriage (51). A PM crystal with no Cs^+ was used as a native dataset. Phenix.AutoSol (51) located seven Cs^+ ions producing an initial mean figure of merit of 0.37 to 3.0 Å resolution; density modification yielded maps with discernible RNA features (Fig. S3B). Phenix.AutoBuild (51) was used to trace the backbone, followed by iterative use of Phenix.refine (51) interspersed with manual building in Coot (55). The resolution of the structure was extended to 2.75 Å resolution using data from an isomorphous crystal with the wild-type *Fpr* sequence. The structure converged on $R_{\text{cryst}}/R_{\text{work}}/R_{\text{free}}$ values of 21.4/21.2/22.8% with acceptable geometry, and a clash score of 1.24 (Table 1). The quality of the refined structure is indicated by the clear electron density for all nucleotides, except a break at positions 34 and 35 within the P3 loop (Fig. S3C). PreQ₁ is visible in omit and unbiased electron density maps that define its placement in the structure (Fig. 2B and Fig. S3A); the ligand-binding pocket is free from crystallographic contacts (Fig. S3F).

Riboswitch MD Simulations. All simulations were conducted using Amber14 with the ff10 force field, which is unchanged for nucleic acids in ff12SB (56–58); a modified force-field parameter was used for improper dihedrals for the exocyclic amine in G•A imino pairs (59). The model was solvated in an isometric box using TIP3P (60). For charge neutralization, 100 Na^+ ions were added, along with 150 Na^+ and 150 Cl^- ions to generate 0.1 M

NaCl (61, 62). The system comprises 139,811 atoms in a $125 \times 125 \times 125$ Å octahedral box. To produce preQ₁, charge and force-field parameters were generated. Hydrogen was added to the methylamine using reduce in AmberTools (63). The RED RESP server (64–66) was used to optimize geometry and to generate atomic point charges at the HF/6–31G* quantum calculation level. Other force-field parameters were obtained using Amber antechamber (67). The model with P5 pairing was subjected to 500 ns of unrestrained MD, and then used as the starting coordinates for four additional ligand-bound MD simulations of 2 μs each; trajectory rmsd values and P4–P5 distances are provided (Fig. S5). Coordinates from Fig. 5 may be obtained from the corresponding author upon request.

SmFRET Analysis. The anti-P5 11-nt DNA oligonucleotide (Fig. S4C, *Inset*) was synthesized chemically followed by desalting (Sigma-Aldrich); the dry pellet was dissolved in polished water as a 0.10 M stock. Experiments that used the anti-P5 DNA strand were examined as described in *Methods*. Briefly, the surface-bound RNA was incubated with smFRET buffer containing the OSS with or without preQ₁ in the presence of 10 μM anti-P5 DNA at room temperature for 15 min before imaging at 16 fps. The control experiments with IXP and 2AP were done on the same quartz slide starting with no ligand, followed by addition of 1 μM each of IXP, 2AP, and preQ₁ in 1 \times smFRET buffer with OSS. Between different ligand titrations, the microfluidic channel was washed with the 1 \times buffer multiple times to remove the free ligand. For all experiments, specific smFRET traces were selected for further analysis provided that they met the following criteria: trace time >6 s; total intensity (donor + acceptor) >300 (arbitrary units); signal-to-noise ratio >5; and single-step photobleaching of Dy-547 and/or Cy5 (Figs. 6B and Figs. S6 A–C and S9 B and C). Dimers were identified and excluded from analysis when smFRET traces exhibited two-step photobleaching of Dy547 and/or Cy5. For each experimental condition, population histograms (Fig. 6C and Figs. S7 A–C, S8 A, C, and G–I, and S9A) were plotted by binning the first 100 frames from each of several hundred molecules. FRET histograms were fit with a sum of Gaussian functions to extract the means and areas of individual peaks using Origin 8.5 (MicroCal). To estimate the kinetics of conformational changes, the smFRET traces were idealized to a two-state model using a hidden Markov model-based segmental *k*-means algorithm as implemented in QuB (68). The cumulative distributions of dwell times in each FRET state were plotted and fitted with exponential functions to obtain the lifetimes in the undocked and docked states, thereby estimating k_{dock} and k_{undock} rate constants (Table 2 and Fig. S6 D–F). The idealized smFRET traces were used to create TODPs using MATLAB as described (69).

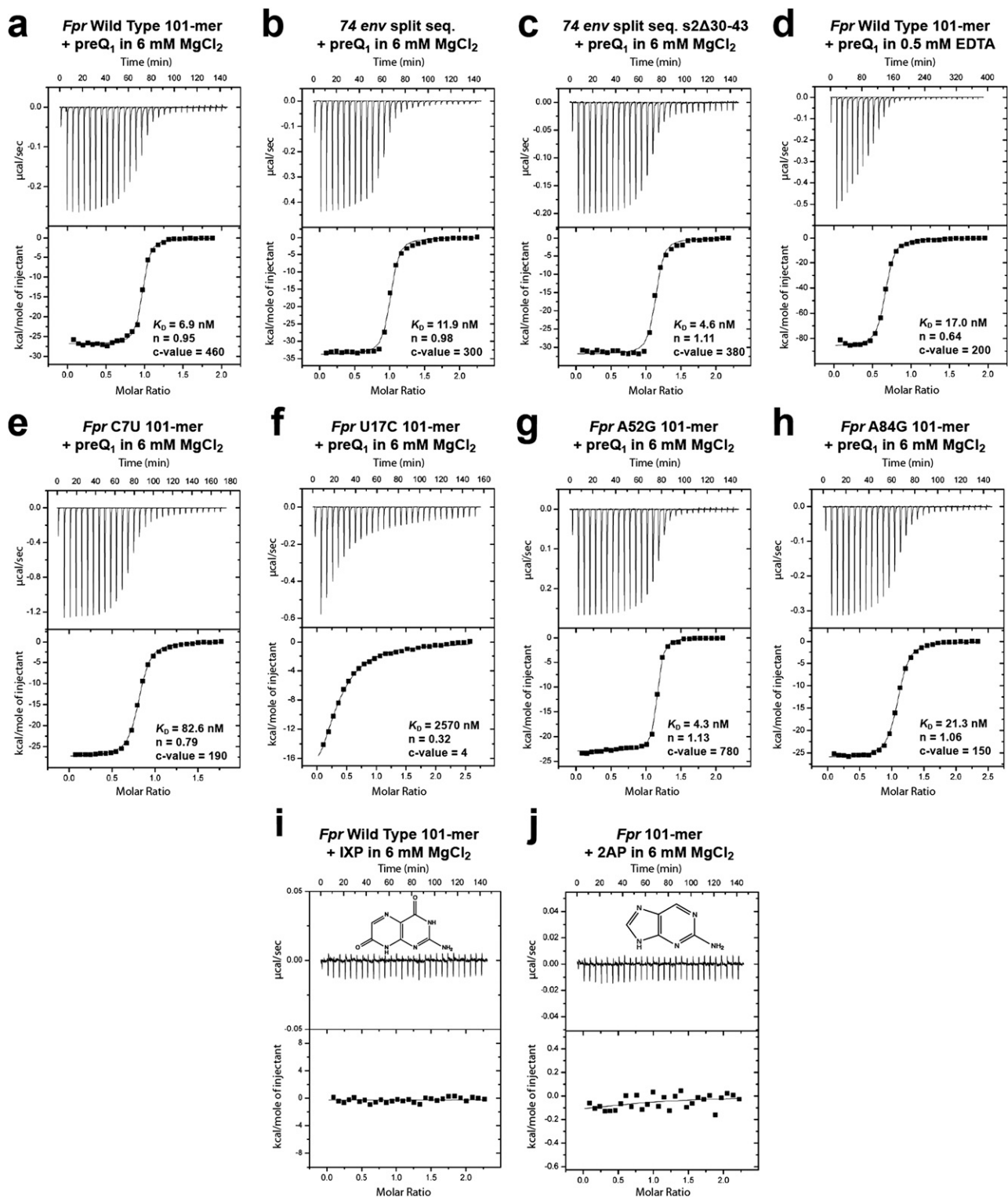


Fig. S1. Representative ITC experiments for preQ₁ binding to preQ₁-III riboswitches. Apparent K_D , stoichiometry values (n), and c values for individual experiments are shown; average values are provided in Table S1. (A) PreQ₁ binding to the wild-type *Fpr* preQ₁-III riboswitch 101-mer (Fig. 1B) in a buffer containing 0.050 M Na-Hepes (pH 7.0), 0.10 M NaCl, 0.006 M MgCl₂; *Methods*. (B) PreQ₁ binding to the split 74 *env* preQ₁-III riboswitch (Fig. S4A). (C) PreQ₁ binding to the 74 *env* preQ₁-III riboswitch in which the 3' end was removed after P2 (s2Δ30-43). (D) PreQ₁ binding to the wild-type *Fpr* preQ₁-III riboswitch, except 0.5 mM EDTA was substituted for MgCl₂ in the buffer used in A. (E) PreQ₁ binding to the C7U mutant in the context of the *Fpr* wild-type riboswitch under conditions described in A. (F) PreQ₁ binding to the *Fpr* U17C mutant as in A. (G) PreQ₁ binding to the *Fpr* A52G mutant as in A. (H) PreQ₁ binding to the *Fpr* A84G mutant as in A. (I) IXP does not bind appreciably to the wild-type preQ₁-III riboswitch under conditions in A. The slightly positive slope of the curve fit could be the result of very weak binding consistent with observations on the wild-type preQ₁-II riboswitch, which shows an apparent K_D for IXP that is ~3 log units poorer than that for preQ₁ (32). (J) 2AP does not bind appreciably to the preQ₁-III riboswitch under buffer conditions described in A. The slightly positive slope of the curve fit could be the result of very weak binding consistent with observations on the wild-type preQ₁-II riboswitch, which shows an apparent K_D for 2AP that is ~3 log units poorer than that for preQ₁ (32).

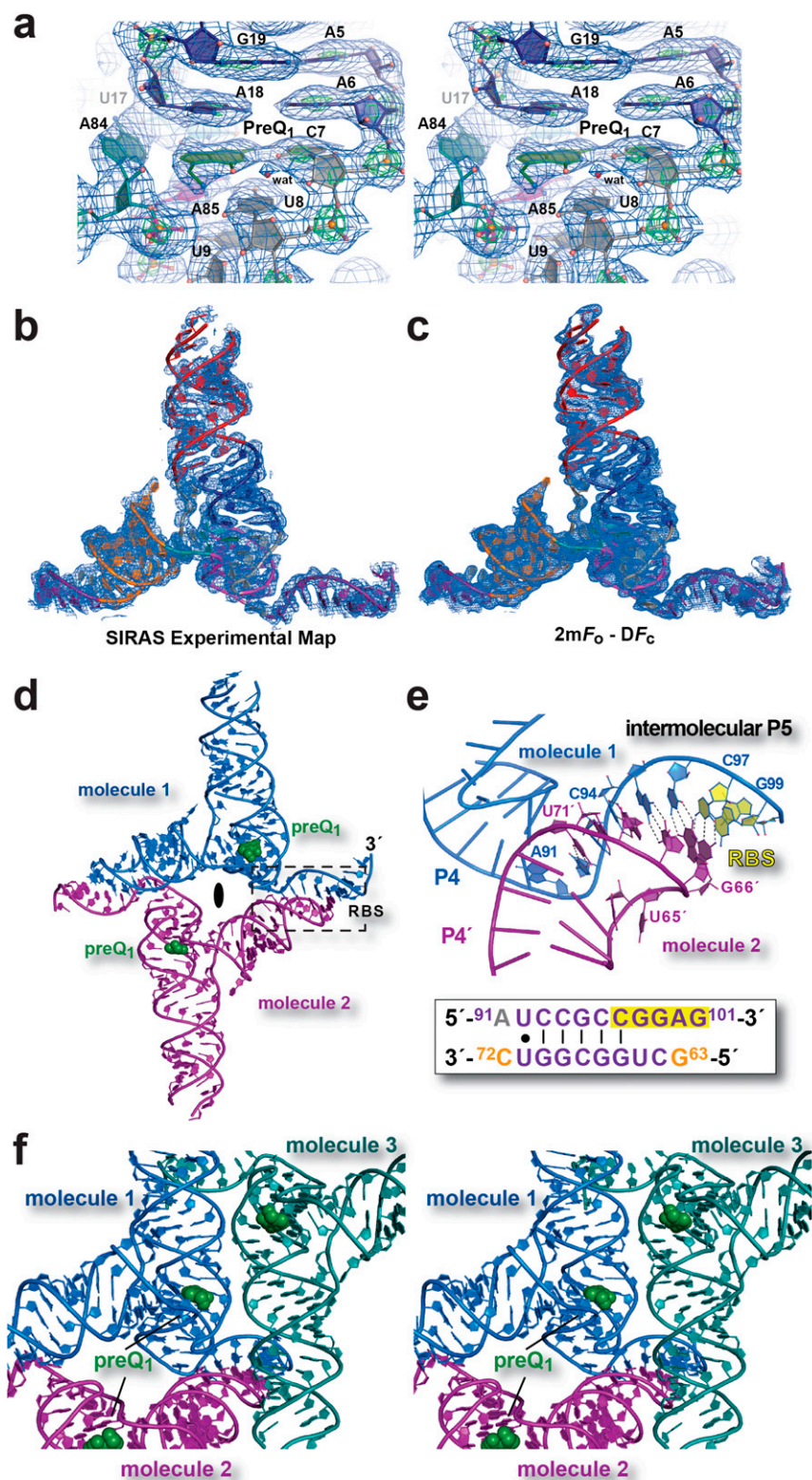


Fig. S3. Representative electron-density maps and crystallographic symmetry interactions of the *Fpr* preQ₁-III riboswitch. (A) Stereoview of the preQ₁-binding site with the final refined structure shown within unbiased, composite iterative-build omit electron density (71) at 2.75 Å resolution; the contour levels are 1.0 σ (blue) and 7.0 σ (green). (B) The 3.0-Å resolution experimental electron density map contoured at 1.0 σ based on the initial density-modified SIRAS phases; a cartoon of the final refined coordinates (Fig. 1C) is included. (C) The final 2.75-Å resolution, reduced-bias (σ_A -weighted) $2mF_o - DF_c$ electron density map contoured at 1.0 σ using phases from the final refined model included as a ribbon diagram (Fig. 1Q). Nucleotides 34 and 35 located in the P3 loop (Top) exhibited poor electron density and were not included in the final model. (D) Ribbon diagram depicting the dyad (filled oval) crystallographic contacts that compose the intermolecular, "domain swapped" region of helix P5. The RBS is labeled and comprises the last five nucleotides of the 3' terminus. (E) Magnified

Legend continued on following page

and maintains the HL_{out}-type pseudoknot as observed in the crystal structure (Fig. 1 *B* and *C*); however, the model indicates P4 bending to an angle of 27° (yellow cone) to form P5. (*D*) Mass-weighted rmsd of all heavy atoms as a function of molecular dynamics simulation time for the model. Atoms for the P3 loop were excluded from the calculation. (*E*) Mass-weighted rmsd of atoms in P5 as function of simulation time based on the trajectories in *D*. P5 is defined by nucleotides 64–70 and 93–99 (Fig. 5*B*), and includes the RBS from position 97–101. (*F*) Intramolecular distance between atom C5 of U77 in helix P4 and atom O3' of G101 in the RBS plotted as a function of simulation time. (*G*) Histogram distribution analysis showing the probability of encountering various U77–G101 distances, denoted (*r*), plotted for the atom pair in *F*. The distance of each peak is labeled. Analysis of trajectories was performed by Ptraj and Cpptraj from AmberTools (67).

